applied sciences

MDPI

Article

Simulation and Experimental Study of the Suppression of Low-Frequency Flow Noise Signals by a Placoid-Scale Skin

Mingxin Cheng [1], Zhijuan Zhu [2,*], Bin Wu [2,*], Lingyun Ye [2] and Kaichen Song [3]

[1] Ocean College, Zhejiang University, Hangzhou 310027, China
[2] College of Biomedical Engineering and Instrument Science, Zhejiang University, Hangzhou 310027, China; lyye@zju.edu.cn
[3] School of Aeronautics and Astronautics, Zhejiang University, Hangzhou 310027, China; kcsong@zju.edu.cn
* Correspondence: zjzhu@zju.edu.cn (Z.Z.); wubinzju@zju.edu.cn (B.W.)

Abstract: This paper addresses the challenge of mitigating low-frequency flow noise signals in autonomous underwater vehicles through the optimization of a placoid-scale skin. Drawing inspiration from the bio-inspired surface features of cylindrical shell structures, an enhanced design of placoid-scale skin is developed using 3D printing technology. This improved structure effectively reduced boundary layer vortices and wake intensity, thereby contributing to the suppression of low-frequency flow noise signals. Experimental results demonstrate that the notable reduction in low-frequency flow noise within the frequency range of 0–500 Hz, with average noise reduction of approximately 5 dB observed at 150 Hz. This reduction is validated by a combination of numerical simulations and experimental testing, confirming the efficacy of the optimized placoid-scale skin in attenuating the low-frequency flow noise associated with uniformly advancing turbulent boundary layers underwater.

Keywords: AUVs; low-frequency flow noise; placoid-scale skin; detectability

check for updates

Citation: Cheng, M.; Zhu, Z.; Wu, B.; Ye, L.; Song, K. Simulation and Experimental Study of the Suppression of Low-Frequency Flow Noise Signals by a Placoid-Scale Skin. *Appl. Sci.* **2024**, *14*, 3855. https://doi.org/10.3390/app14093855

Academic Editor: Tomasz Figlus

Received: 29 February 2024
Revised: 25 April 2024
Accepted: 29 April 2024
Published: 30 April 2024

Copyright: © 2024 by the authors. Licensee MDPI, Basel, Switzerland. This article is an open access article distributed under the terms and conditions of the Creative Commons Attribution (CC BY) license (https://creativecommons.org/licenses/by/4.0/).

1. Introduction

The challenging and intricate nature of oceanic environments complicates direct human intervention in surveys. Therefore, autonomous underwater vehicles (AUVs) have become vital tools for achieving efficient and convenient oceanic monitoring [1]. Equipped with a variety of sensors, AUVs can perform diverse tasks in civilian applications, including mine surveys, environmental monitoring, underwater equipment maintenance, and hydrological surveys [2–4]. In the execution of underwater exploration research, the turbulent boundary layer (TBL) and turbulent interference occur in AUVs due to the high Reynolds numbers and complex oceanic environments. The flow noise caused by AUVs not only increases energy consumption during the working process, but also undermines their accuracy and system stability, thereby decreasing the signal-to-noise ratio as the propulsion speed increases [5–8]. Additionally, along with gradually reducing the mechanical noise of AUVs, flow noise has become one of the main sources of noise. Further studies indicate that low-frequency vibrations induced by flow noise reduce the stability of marine engineering equipment and compromise its stealth characteristics, thereby increasing the risk to sustainable development [9–11]. Therefore, in order to further enhance the requirements of geological exploration, it is necessary to reduce the flow noise of AUVs.

The current research on mitigating the flow noise of AUVs is primarily classified into two categories. Some researchers approach the problem by employing structural designs that aim to diminish resistance and subsequently flow noise as the AUVs progresses. Notably, Fan Y [12] utilizes the study and modeling of the physical dimensions of the humpback whale to propose a bionic hull shape for AUVs. This design is purported to be highly suitable for extended-distance and high-speed applications. Additionally, Hu

F [13] conceptualized a multidisciplinary design optimization framework and applied it to a 200 kg AUV with the goal of maximizing its endurance. Piskur P [14] designed a single flexible side fin with adequate proportions and stiffness for the energy-saving propulsion system of biomimetic unmanned underwater vehicles, further improving the mechanical performance of the system. Researchers have focused on the overall structural design of AUVs, reducing overall flow noise from a structural design perspective.

Nowadays, biomimetic surfacing, designs that replicate the morphology of biological surfaces, has been introduced to reduce flow noise. Researchers utilize bionic design approaches to modify the skin of the interaction surface, aiming to reduce low-frequency flow noise. Li W [15] reports on the experimental investigation of the effect of sinusoidal riblets on the near-wall characteristics of the TBL. Direct numerical simulation results demonstrate a notable decline in energy levels at separation area [16]. In the comparative analysis of flow and noise control studies, Joslin, R.D [17] concluded that micro-grooves could decrease drag, and speculated that a reduction in TBL energy could subsequently result in a decrease in internal noise. The initial research exploring noise reduction with micro-grooving was conducted by Gillcrist, M.C and Reidy, L.W [18], researchers have applied micro-groove surface coatings to ships to conduct experiments on drag reduction and noise minimization, and obtained noise reduction results. Later, Shi, X [19] utilized the Northwestern Polytechnical University's water hole to investigate flow noise from underwater vehicles with biomimetic surfaces, where researchers found that noise reduction could reach up to 5 dB.

In research aimed at reducing flow noise by utilizing surfaces as research objects, several comprehensive studies have delved into many noise reduction technologies derived from shark skin [20,21]. There has been increasing number of studies on the drag reduction properties of shark skin's micro-grooved surface in recent years, with most focusing primarily on investigating flow field characteristics and resistance properties [22–24]. From the acoustical properties of shark skin, Meng K [25] establishes a correlation between drag and noise reduction; the conclusion shows that the grooved structure reduces resistance and can also reduce flow noise by about 2 dB. Dang Z [26] devised an innovative method for flow noise reduction based on shark skin, and conducted a numerical simulation of the hydrodynamic noise of three-dimensional hydrofoils, showing flow noise can be reduced by about 3 dB. Therefore, a micro-groove surface can contribute to the stability of the flow field, reducing flow noise by approximately 2–3 dB according to recent studies. For AUVs utilized in terrain exploration, the flow noise generated during the operation significantly affects their operational stability. Moreover, low-frequency high-energy noise can not only cause equipment damage but can also increase the difficulty of exploration, thereby reducing the exploration range of AUVs. Decreasing the energy consumption, increasing the exploration range of AUVs, and enhancing terrain exploration necessitates further research into the low-frequency flow noise of AUVs to mitigate TBL flow noise.

In this paper, we primarily focus on the cylindrical shell of AUVs and employ a combination of experimental and numerical simulation to explore the relationship between the TBL and low-frequency flow noise in the flow field, providing new insights for the research of low-frequency flow noise reduction technologies for AUVs. To further refine the research, high-precision 3D printing methods with continuous digital light manufacturing technology were used to replicate the structure and details of the placoid scales [27,28]. In additionally, to reveal the correlation between the flow field and low-frequency flow noise, the large eddy simulation (LES) method was selected as the numerical simulation method for the flow field, which has exhibits good performance in terms of calculating complex turbulent processes [29,30]. In summary, via a combination of numerical simulations and experimental testing, this paper proposes improved methods for the suppression of low-frequency flow noise generated by the cylindrical shell structure of AUVs.

The other sections of this article are as follows: In Section 2, via the derivation of the energy equation and Green's function, the basic theory of sound pressure calculation is determined. In Section 3, the characteristics of the placoid scales are described, and the high-strength material RC30 is utilized for high-precision processing of the placoid-

scale skin. In Section 4, different types of flow fields over placoid-scale skin, riblet skin, and smooth skin are compared via numerical simulation, and the principle of reducing flow noise by placoid-scale skin through the distribution of the flow field is described. In Section 5, the experimental design and measurement of low-frequency flow noise are completed. The conclusions are drawn in Section 6.

2. Theory and Derivation

The wave equation of a perfect fluid can be decomposed into three constituent elements: the mass conservation equation, the Euler equation, and the adiabatic equation of state. Moreover, these elements encapsulate the adiabatic relationship between pressure and density, as follows [31]:

$$\frac{\partial \rho}{\partial t} = -\nabla \cdot \rho v \tag{1}$$

$$\frac{\partial v}{\partial t} + (v \cdot \nabla)v = -\rho^{-1}\nabla p(\rho) \tag{2}$$

$$p = p_0 + p'\left[\frac{\partial p}{\partial \rho}\right]_S + \frac{1}{2}(p')^2\left[\frac{\partial^2 p}{\partial \rho^2}\right]_S \tag{3}$$

Here,

$$c^2 = \left[\frac{\partial p}{\partial \rho}\right]_S \tag{4}$$

where, ρ denotes the density, v denotes particle velocity, and p denotes the pressure, and p' denotes the pressure fluctuation. The subscript S indicates the requirement to take the thermodynamic partial derivative under isentropic conditions. Combing Equations (1) and (4), the relationship can be shown as follows [31]:

$$\frac{\partial \rho'}{\partial t} = -\nabla \cdot (\rho_0 v) \tag{5}$$

$$\frac{\partial v}{\partial t} = -\frac{1}{\rho_0}\nabla p'(\rho) \tag{6}$$

$$\frac{\partial p'}{\partial t} = c^2\left(\frac{\partial \rho'}{\partial t} + v \cdot \nabla \rho_0\right) \tag{7}$$

If ρ_0 is constant, Equation (7) can be rewritten as:

$$p' = \rho' c^2 \tag{8}$$

With real-world conditions, the hydrological environment exhibits significant variability. Consequently, it is posited that liquid density ρ_0 and sound velocity c are as temporally invariant as temperature. Furthermore, liquid density and sound velocity do not fluctuate over t. Equation (5) and Equation (6) are combined to derive the wave equation. By altering the order of operations in the derivation and applying Equation (7), sound pressure can be written as follows:

$$\rho \nabla \cdot \left(\frac{\nabla p}{\rho}\right) - c^{-2}\frac{\partial^2 p}{\partial t^2} = 0 \tag{9}$$

According to Equation (9), if ρ is constant in time and space, the standard sound pressure wave equation is shown as follows:

$$\nabla^2 p - c^{-2}\frac{\partial^2 p}{\partial t^2} = 0 \tag{10}$$

Equations (5) and (6) can be taken to derive the wave equation of particle velocity under the unidirectional propagation of sound waves, is shown as follows [32]:

$$\rho^{-1}\nabla\left(\rho c^2\nabla\cdot v\right)-\frac{\partial^2 v}{\partial t^2}=0 \tag{11}$$

Equation (11) can be transformed into a scalar wave equation by introducing ϕ:

$$v=\nabla\phi \tag{12}$$

By incorporating the density invariant condition ($\nabla\rho=0$) in Equation (12) and the sound pressure solution process into Equation (11), the following relationship can be obtained as follows:

$$\nabla\left(c^2\nabla^2\phi-\frac{\partial^2\phi}{\partial t^2}\right)=0 \tag{13}$$

In addition, the ϕ meet the following conditions:

$$\nabla^2\phi-c^{-2}\frac{\partial^2\phi}{\partial t^2}=0 \tag{14}$$

Using the relationship between velocity and displacement $v=\partial u/\partial t$, the displacement potential ψ is defined as follows:

$$u=\nabla\psi \tag{15}$$

Combined with Equations (10) and (14), the wave equation of the displacement potential can be written as follows:

$$\nabla^2\psi-c^{-2}\frac{\partial^2\psi}{\partial t^2}=0 \tag{16}$$

The kinematic relationships of Equations (5), (7), and (15) can show the sound pressure equation in terms of displacement potential, which is as follows:

$$p=-K\nabla^2\psi \tag{17}$$

In Equation (17), K is defined as the bulk elastic modulus. Here:

$$K=\rho c^2 \tag{18}$$

In addition, Equation (18) is the basic equation for ideal linear elastic fluids. Combining Equations (16) and (18), the relationship can be calculated as follows:

$$p=-\rho\frac{\partial^2\psi}{\partial t^2} \tag{19}$$

Hence, once the equation of the displacement potential is solved, the sound field of a fluid in a uniform medium can be obtained. Subsequently, the sound pressure level at the specified point can be established based on Equation (19).

For the purpose of solving the wave equation, the displacement potential should be added into the source strength of the bounded medium model. $f(r)$ denotes the volume in the sound field, the displacement potential function $\psi(r)$ satisfies the non-homogeneous Helmholtz equation [32]:

$$\left[\nabla^2+k^2\right]\psi(r)=f(r) \tag{20}$$

where, $k=k(r)$ represents the wavenumber variable of the medium.

The Green's function for solving the Helmholtz equation is defined as follows:

$$g_\omega(r,0) = \frac{e^{ikr}}{4\pi r} \tag{21}$$

In general, when the sound source is at $r = r_0$, the Green function can be expressed as follows:

$$g_\omega(r,r_0) = \frac{e^{ikr}}{4\pi R}, R = |r - r_0| \tag{22}$$

In the process of solving Equation (20), the generalized Green's function is introduced:

$$G_\omega(r,r_0) = g_\omega(r,r_0) + H_\omega(r) \tag{23}$$

In Equation (23), $H_\omega(r)$ is an arbitrary function that satisfies the homogeneous Helmholtz equation as follows:

$$\left[\nabla^2 + k^2\right] H_\omega(r) = 0 \tag{24}$$

Thus, Equation (20) being satisfied by the generalized Green's function can be expressed as follows:

$$\left[\nabla^2 + k^2\right] G_\omega(r,r_0) = -\delta(r - r_0) \tag{25}$$

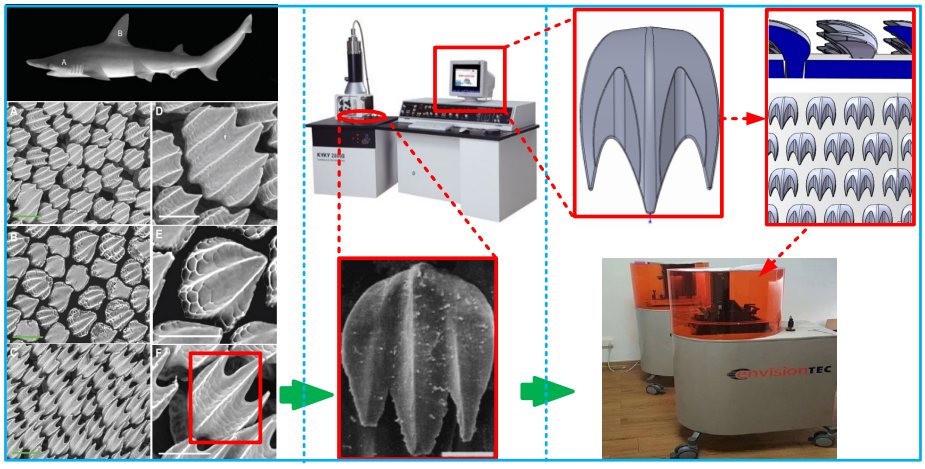
Combing Equation (20) by $G_\omega(r,r_0)$ and Equation (25) by $\psi(r)$, the sound source in a uniformly bounded medium can be obtained as follows:

$$\psi(r) = \int_S \left[G_\omega(r,r_0)\frac{\partial\psi(r)}{\partial n_0} - \psi(r_0)\frac{\partial G_\omega(r,r_0)}{\partial n_0}\right] dS_0 - \int_V f(r_0)G_\omega(r,r_0)dV_0 \tag{26}$$

where, n_0 is the outward normal on the surface. Equation (26) represents the minimization of $\psi(r)$, indicating that the intensity of sound field fluctuations can be reduced, thereby lowering the sound pressure level.

3. Skin Design and Manufacture

Recent studies have highlighted the impressive swimming speed and drag reduction capabilities of fast-swimming sharks, leading to several significant implications. Researchers have extensively studied shark characteristics such as mucus, placoid scales, and streamlining [33,34]. Afroz F [35] conducted tests on shark skin within an water tunnel, concluding that shark skin can modulate both laminar flow and turbulent separation. Figure 1a presents an in-depth view of shark's skin placoid scales via ESEM images [36].



(**a**) (**b**) (**c**)

Figure 1. Fast-swimming shark skin manufacture. (**a**) ESEM images [33], (**b**) scan data, (**c**) model reconstruction.

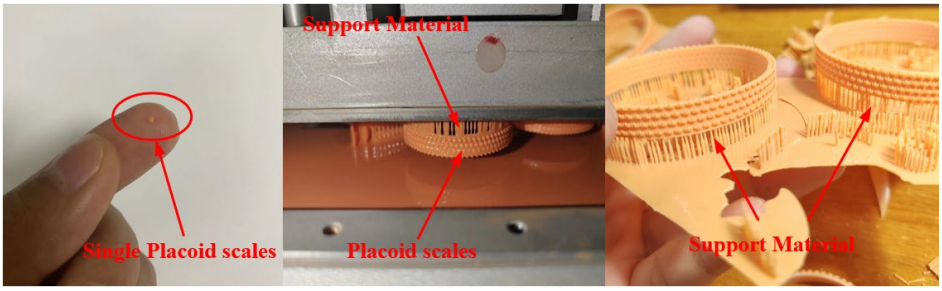
In Qingdao, China, fishermen recently captured a deceased short-finned horse shark. The dry skin sample was placed in a scanning electron microscope for observation and measurement. From the scanning results, researchers selected a representative shield tunneling scale structure [37]. Thus, placoid scales can be used to reconstruct a model, as illustrated in Figure 1b.

Many scholars have studied the manufacturing process of the placoid scales of fast sharks. In addition to more traditional methods, such as computer numerical control, biomimetics is gradually becoming a research topic. Based on the microscopic structure of shark skin, Liu Y [38] initially replicated the surface of shark skin on Polydimethylsiloxane film and achieve a drag reduction rate of 21.7% on the biomimetic surface. Figure 1c illustrates the 3D printer, and the reconstructed placoid-scale model is recreated, as illustrated in Figure 1c. Table 1 shows the properties of RC30.

Table 1. Material properties of high-temperature resins.

Description	Tensile Strength	Elongation at Break	Flexural Strength	Flexural Modulus
RC30	46 MPa	2.5%	102 MPa	3860 MPa

In this paper, to reconcile actual requirements and machining precision, we have increased the placoid scales by approximately 10 times. This scaling ensures precision in processing and results in a placoid-scale morphology characterized by distinct three-dimensional features. The 3D printing process of the placoid scales is depicted in Figure 2, with the individual placoid scales in Figure 2a and the completed product in Figure 2b. The support materials utilized during the 3D printing process are depicted in Figure 2c.



(**a**) (**b**) (**c**)

Figure 2. Three-dimensional printing of placoid-scale skin (a single placoid scale is shown in (**a**)). (**a**) Placoid scales, (**b**) sample preparation, (**c**) support material.

In this study, the flow noise reduction effect is assessed via outdoor experiments. In these experiments, the cylindrical shell is constructed from nylon, measuring 500 mm in length, and with a diameter (D1) of 50 mm, as illustrated in Figure 3. For more intuitive comparison of the skin, Figure 4 illustrates smooth cylindrical shells, ribbed skin cylindrical shells, and placoid-scale skin cylindrical shells.

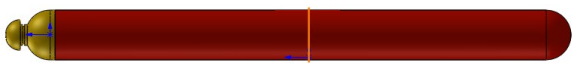


Figure 3. Cylindrical shell.

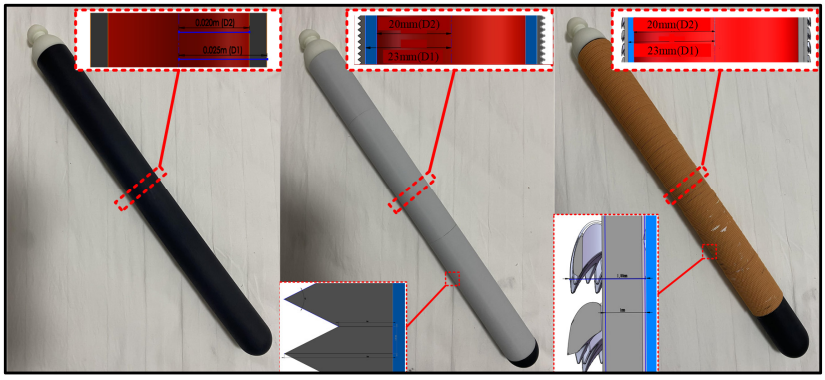


Figure 4. Processed products for different skin types.

4. Numerical Simulation Results and Analysis

In this study, the Reynolds number (Re) of the cylindrical shell is about 50,000, indicating turbulent flow within the TBL. Turbulent motion is characterized by its irregularity, nonstationary, and multidimensional nonlinearity. These characteristics amplify the complexity of TBL turbulent motion and pose challenges for numerical simulation. Therefore, the LES method is employed as the turbulence model for numerical simulation. By filtering turbulence, LES achieved better numerical simulation accuracy. Turbulence is characterized by two distinct scales of eddies including both large-scale and small-scale. Large-scale eddies primarily govern the energy and momentum transfer in turbulence, while small-scale eddies are less affected by boundaries. Thus, higher accuracy in boundary layer turbulence under complex conditions can be attained [39].

4.1. Simulation Setup

The LES is chosen for the numerical simulation of turbulence in the overlapping grid partitioning process, offering enhanced calculation accuracy. In this study, the inlet velocity is set to 0.833 m/s, the outlet is subjected to a normal pressure gradient of 0, and the far-field boundary is expanded to 10 times the diameter of the target, effectively mitigating wall effects on the flow field. Additionally, the flowing medium is water, and the density and kinematic viscosity are updated accordingly.

In the simulations, selection of the turbulence model for the LES was carried out using the Smagorinsky–Lilly subgrid-scale model. The semi-implicit method for pressure linked equations consistent algorithm was employed for coupling pressure and velocity. For pressure spatial discretization, the pressure staggering option algorithm was used, while the bounded central differencing algorithm was applied for momentum calculations.

Table 2 illustrates that as grid resolution improves, the friction resistance coefficient (C_f) of the AUVs approaches convergence. When the number of grids exceeds 2.07 million, the C_f remains relatively stable. Therefore, this article utilizes a 2.07 million grid for numerical simulation.

Table 2. Results of grid convergence analysis.

Description	Grid 1	Grid 2	Grid 3	Grid 4	Grid 5	Grid 6
Grid number	6.8×10^5	1.15×10^6	1.62×10^6	1.90×10^6	2.07×10^6	2.27×10^6
C_f	0.09967	0.09407	0.09041	0.08953	0.08952	0.08951

4.2. Simulation Analysis

Figure 5a shows the pressure distribution of the smooth, riblet, and placoid-scale skin in the flow fields.

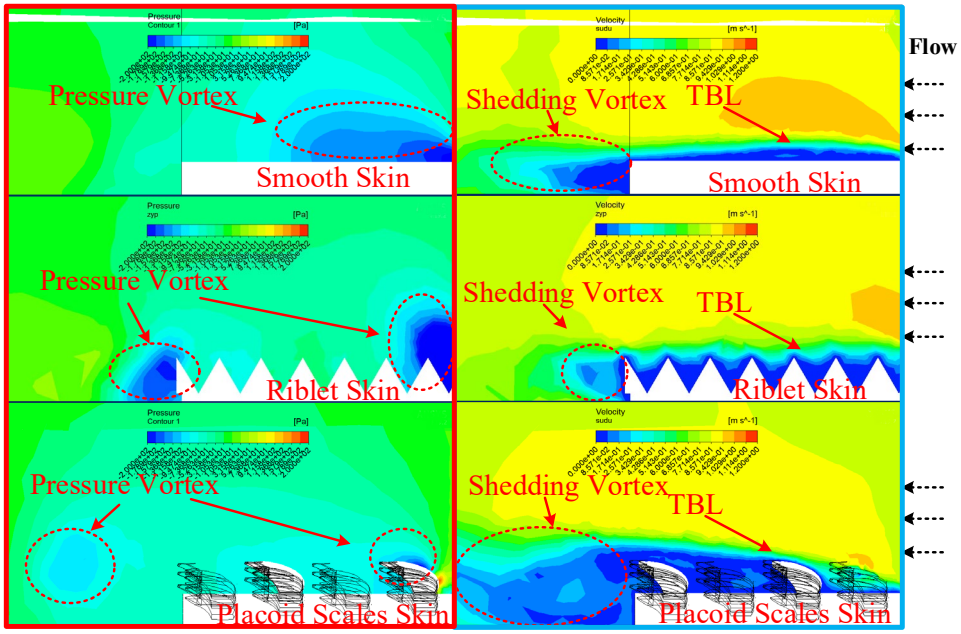


Figure 5. Pressure distribution and velocity distribution. (**a**) Pressure distribution, (**b**) velocity distribution.

In Figure 5, the three skins generate pressure vortices of varying sizes (highlighted by red circles in Figure 5a). The presence of these pressure vortices can lead to disparities in pressures across different regions, subsequently influencing structural vibration and other factors. Smooth skin produces a pressure vortex with substantial negative-pressure regions at its core, which may result in intense vibrational effects and potentially severe fluctuations in sound pressure. This may lead to an increase in low-frequency flow noise. In contrast, both riblet skin and placoid-scale skin transform larger single-pressure vortices into two separate negative-pressure regions (indicated by red circles in Figure 5a). The reduction in pressure vortices is more pronounced for placoid-scale skin as its negative-pressure region and numerical values are considerably diminished.

The velocity distribution in the flow fields of smooth, riblet, and placoid-scale skin is shown in Figure 5b.

The velocity distribution enables the observation of speed changes between the different skin types, providing a more direct representation of shedding vortices. The three skins exhibit certain degrees of shedding vortex. Smooth skin has the strongest intensity, with highly concentrated regions of shedding vortices. Placoid-scale skin demonstrates larger shedding vortex regions, but with an evident decrease in intensity compared to smooth skin. Riblet skin exhibits the weakest shedding vortex, characterized by smaller regions and significantly lower intensity. The riblet skin reduces the shedding vortices level by level, resulting in a weaker vortex.

Upon examining the TBL of the three skin types, it becomes apparent that thickness follows specific pattern: placoid-scale skin has the lowest thickness, followed by smooth skin, while riblet skin possesses the highest thickness. The varying TBL thickness also highlights the effect of passive fluid control on the three skins, which is demonstrated by the strength of nonlinear changes when a fluid flows through structural surfaces. The numerical simulation results suggest that placoid-scale skin should have a more pronounced effect on reducing flow noise.

To illustrate the vortex alterations as fluid flows through various skin surfaces, Figure 6 presents the vortex diagrams for the flow fields of smooth, riblet, and placoid-scale skin.

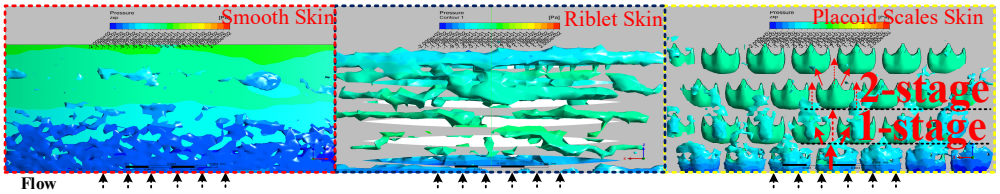


Figure 6. Vortex distribution. (**a**) Smooth skin, (**b**) riblet skin, (**c**) placoid-scale skin.

The vortex distribution provides comprehensive and intuitive visualization of the vortex generation and dissipation process of various structural surfaces. The vortex distribution for both smooth skin and riblet skin exhibits a decreasing trend from the inflow to the outflow direction, accompanied by a gradual reduction in vortex intensity along the surface. In the vortex diagram of the placoid-scale skin, the vortex weakens through two distinct stages (labeled 1 and 2 in Figure 6c).

5. Experiments and Discussions

5.1. Experiment Design

The experiment was conducted in Thousand Island Lake, Zhejiang Province, China. Following preliminary investigation, the northwestern lake area of Thousand Island Lake was selected because it is not a primary navigation channel and exhibits fewer background noise interferences. The majority of the experiment area has a depth of approximately 40 m, with a maximum depth of approximately 60 m. Figure 7 illustrates the experiment environment.

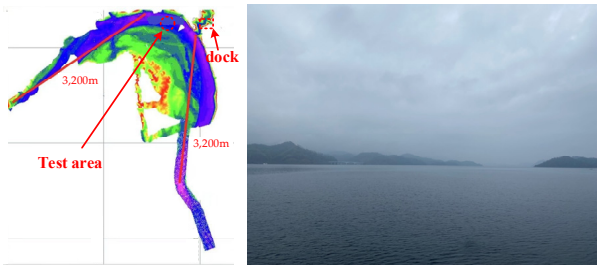


Figure 7. Thousand Island Lake experiment area.

The experimental apparatus primarily consisted of a constant-speed winch, an RHCA-14 hydrophone, a signal acquisition card, a dedicated hydrophone power supply, and a PC, as partially depicted in Figure 8a. The experimental sketch is illustrated in Figure 8b. The hydrophone exhibited several parameters, which were as is shown in Table 3.

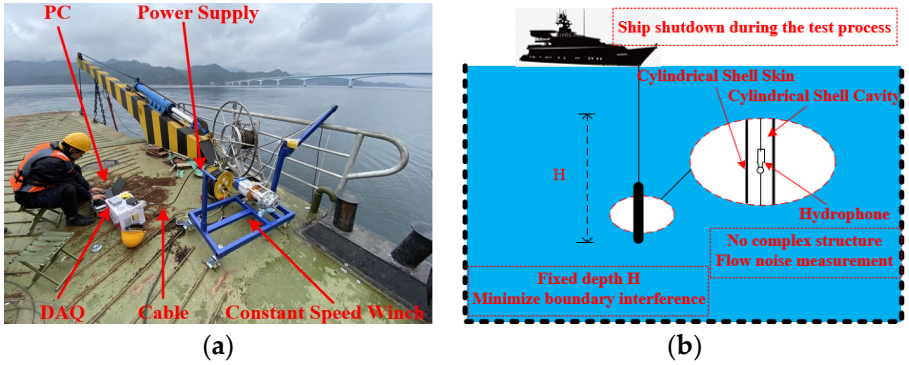


Figure 8. Experiment design. (**a**) Experiment equipment, (**b**) experiment sketch.

Table 3. RHCA-14 hydrophone parameters.

Operating Frequency Range	Linear Frequency Range	Low Frequency Sensitivity	Horizontal Directional-ity	Vertical Beam Opening Angle	Direct Capacitance
0 Hz~100 kHz	20 Hz~80 kHz	−202 dB ± 1 dB @250 Hz	±1.5 dB @100 kHz	68° ± 2° @100 kHz	11 nF ± l nF

During the experiment, the constant-speed winch raised three types of cylindrical shells with varying skin (smooth, riblet, and placoid scales) at a fixed speed (0.833 m/s). The experiment process in Figure 9a, and different skin objects are shown in Figure 9b.



Figure 9. Experiment process and objects. (**a**) Experimental process, (**b**) different skins.

In the experiment, the flow noise signal was recorded by hydrophones and subsequently collected by data acquisition cards. These signals were then converted into a digital format within the acquisition card before being stored on the PC. To ensure accuracy and mitigate potential errors, multiple measurements were performed during the experiment, as illustrated in Figure 10.

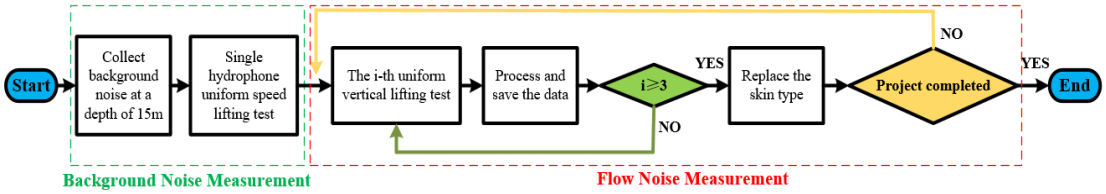


Figure 10. Experiment process diagram.

5.2. Experiment Results and Discussions

Prior to the experiment, the tester conducted preliminary assessment of the environmental noise and performed tests on the hydrophone. The background noise measurements are shown in Figure 11, with the blue curve representing the environmental noise results before the start of the experiment, and the red curve representing the results at the end of the experiment.

Figure 11a illustrates the results of background noise measurements at 0–500 Hz for the hydrophone, while Figure 11b illustrates the envelope results of the noise spectrum. This consistency suggests that both the experiment environment and the electronic equipment were relatively stable.

In the experiment, flow noise measurements were conducted on the cylindrical shells with different skin types. The experimental results are illustrated in Figures 12–14, respectively.

The comparison results between smooth skin and the riblet skin are illustrated in Figure 12, where the blue curve represents the smooth skin and the red curve represents the riblet skin. In the 0–500 Hz range, the riblet skin demonstrated a notable reduction in low-frequency flow noise at 72 Hz, achieving a noise reduction of more than 4 dB. This indicates that flow noise may be influenced by factors such as the structure of the riblet skin.

Figure 13 presents the comparison between the smooth skin and the placoid-scale skin. The blue curve represents the smooth skin, while the red curve represents the placoid-scale skin. In the 10–450 Hz range, the placoid-scale skin significantly reduced low-frequency flow noise, with a reduction of 5 dB observed at 150 Hz. However, between 450 and 500 Hz, the placoid-scale skin increased the flow noise.

In Figure 14, seeking to provide an intuitive comparison between the riblet skin and the placoid-scale skin, it can be observed that riblet skin exhibits superior noise reduction performance below 140 Hz. Conversely, in the frequency range of 140–500 Hz, the flow noise reduction effect of the placoid-scale skin surpasses that of the riblet skin.

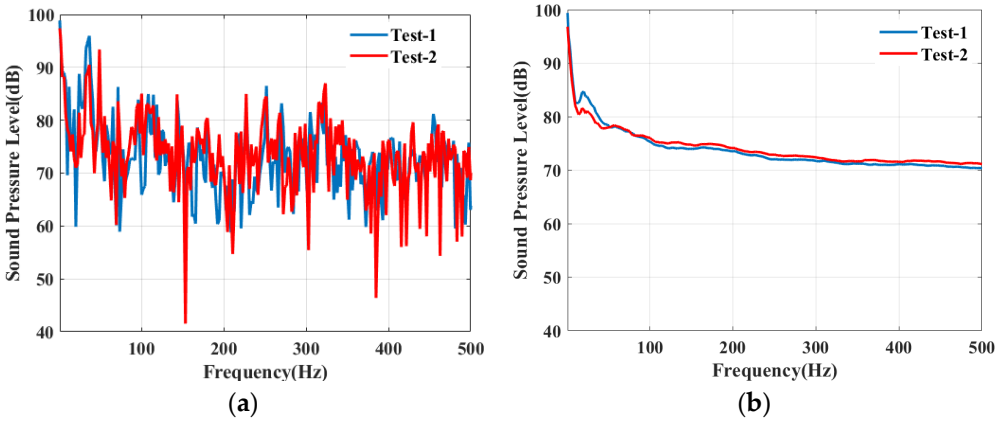


Figure 11. Background noise of the experiment. (**a**) Experimental data, (**b**) envelope diagram.

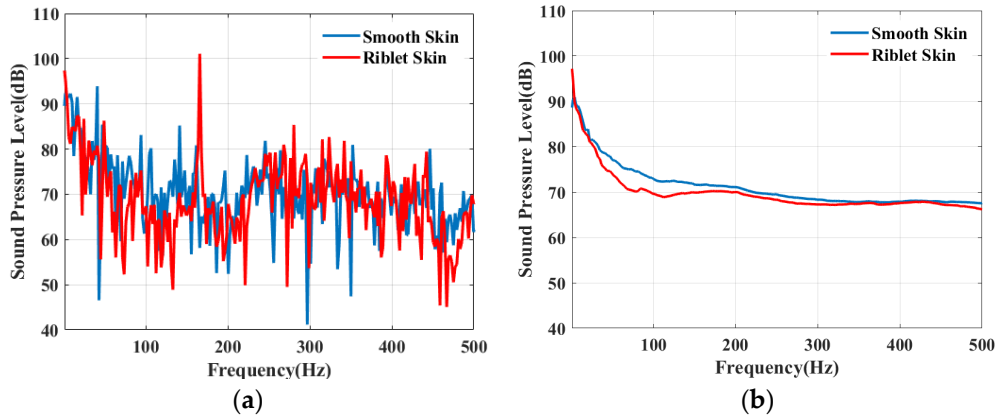


Figure 12. Comparison of smooth and riblet skin flow noise. (**a**) Experimental data, (**b**) envelope diagram.

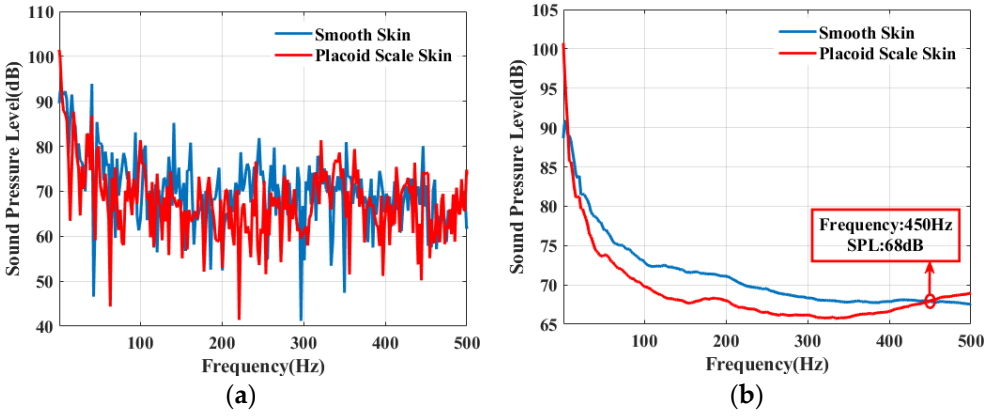


Figure 13. Comparison of smooth and placoid-scale skin flow noise. (**a**) Experimental data, (**b**) envelope diagram.

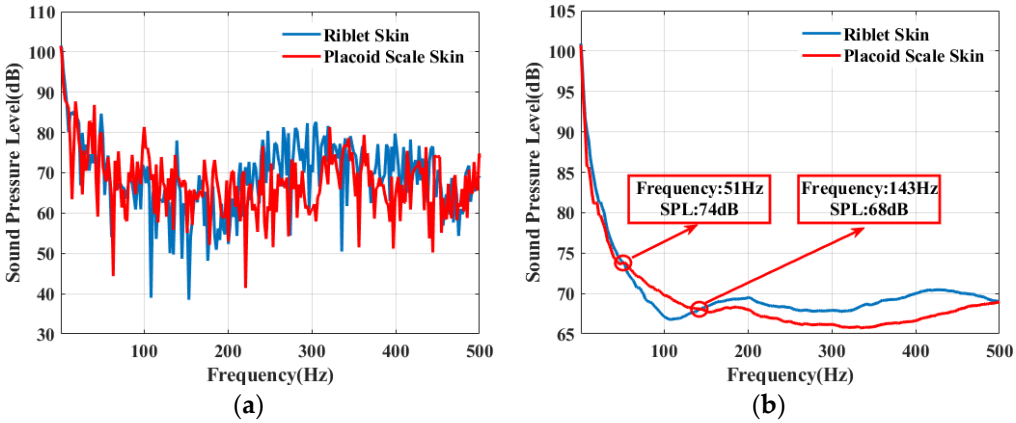


Figure 14. Comparison of riblet and placoid-scale skin flow noise. (**a**) Experimental data, (**b**) envelope diagram.

5.3. Sensitivity Measurement Experiment Results and Discussion

In Section 5.2, it was observed that both the riblet skin and the placoid-scale skin exhibit superior performance in flow noise reduction compared to the smooth skin. To further determine whether the flow noise measurement results of the experiment stemmed from the structural design, the sensitivity measurement experiment for the hydrophones was devised.

In this experiment, different hydrophone sensitivities are measured by replacing the cylindrical shell with smooth skin, riblet skin, and placoid-scale skin, respectively. The sensitivity measurement experiment was conducted at Zhejiang University, with sketches and some physical objects depicted in Figure 15.

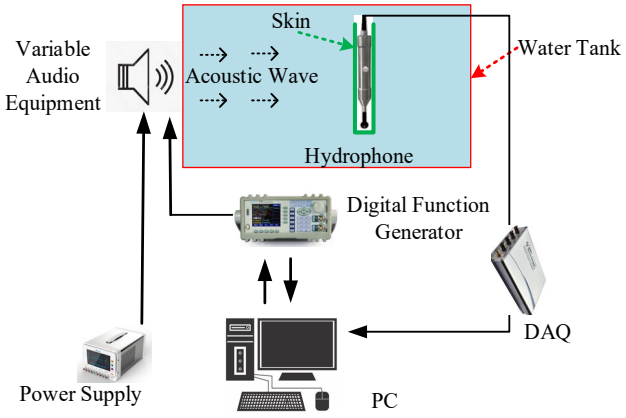


Figure 15. Sensitivity calibration experiment sketch.

In this experiment, the paper presents the results for the representative frequencies of 111 Hz and 313 Hz. These results are illustrated in Figures 16–18.

In the sensitivity measurement experiment, the frequencies of 111 Hz and 313 Hz were observed under power supplies of 10 mV and 50 mV. Using a standard smooth-skin cylindrical shell as reference, it was noted that at 111 Hz and 313 Hz, the rates of change for the riblet skin surface cylindrical shells were 11.82% and 14.49%, respectively. In contrast, the rates of change for the placoid-scale skin cylindrical shells were 2.08% and 0.69%. This observation leads to the conclusion that the covering material of the riblet skin cylindrical shells has a much more detrimental effect on the sound pressure level.

By combining the flow noise experiment and the sensitivity measurement experiment, the effects of flow noise reduction for the different types of skin can be obtained. The results of the flow noise measurement experiment and the sensitivity measurement experiment for the different skin types are presented in Table 4.

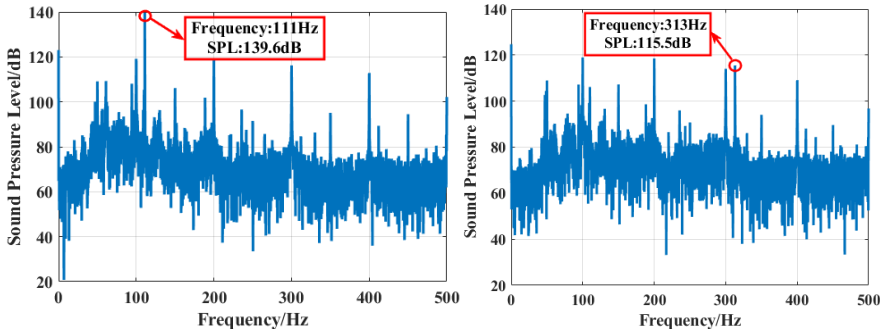


Figure 16. Sensitivity measurement for smooth skin at 111 Hz and 313 Hz.

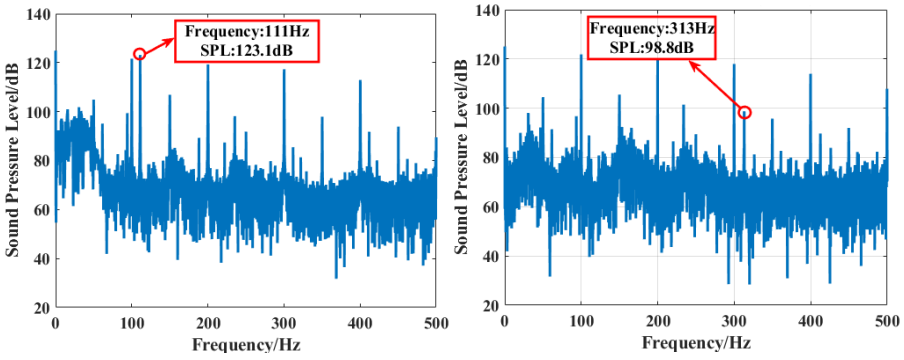


Figure 17. Sensitivity measurement for riblet skin at 111 Hz and 313 Hz.

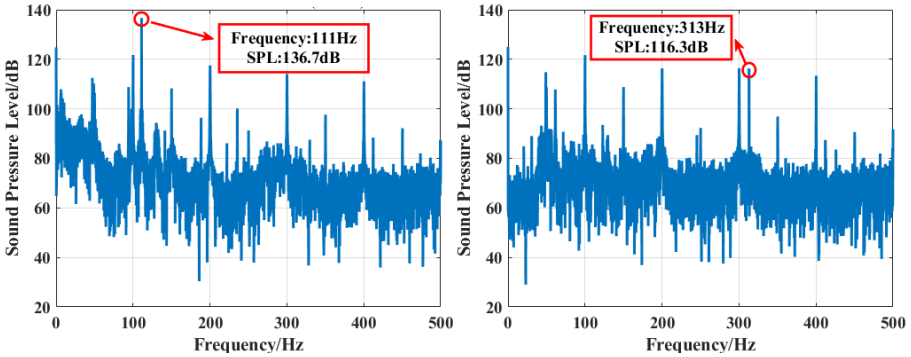


Figure 18. Sensitivity measurement for placoid-scale skin at 111 Hz and 313 Hz.

Table 4. Different skin flow noise and sensitivity measurements.

Type	Reduction Range (Hz)	Reduction Capability (dB)	Measuring Error (111 Hz)	Measuring Error (313 Hz)
Smooth Skin	/	/	/	/
Riblet Skin	0–500	4	11.82%	14.49%
Placoid-Scale Skin	0–450	5	2.08%	0.69%

Consequently, the analysis of reducing flow noise by riblet skin cylindrical shells in Section 4 is deemed inaccurate. The primary factor contributing to flow noise reduction during the experiment is not solely attributed to a decrease in surface turbulence intensity. In fact, in the experimental study, the results of reducing flow noise by riblet skin are influenced by the material properties or structural characteristics of the riblet skin. This provides useful insights for reducing flow noise.

In contrast, the material (high-temperature resins) of the placoid-scale skin cylindrical shells exhibits favorable sound transmission characteristics. This finding substantiates

that, compared to smooth skin, placoid-scale skin can effectively decrease low-frequency flow noise by targeting a boundary layer turbulence intensity reduction. In the process of flow noise reduction by placoid-scale skin, the numerical simulation results showed that the placoid scales can further reduce the intensity of the turbulent boundary layer by weakening the pressure vortex, thereby reducing the flow noise of AUVs. This conclusion is verified by the experimental results for the placoid-scale skin.

6. Conclusions

In this study, an approach of designing and processing different types of skin using 3D printing and novel materials is proposed, aiming to enhance the detectability of AUVs. Analysis of the numerical simulation results reveals that the placoid-scale skin effectively diminishes the intensity of boundary-layer eddies and wake flows by controlling the turbulent flow of the cylindrical shell structure of the AUV. Three types of skins were installed on the outer surface of the cylindrical shell structure, and the effectiveness in suppressing flow noise was assessed through experiments. The experimental results demonstrate that both riblet skin and placoid-scale skin contribute to reducing flow noise in circular cylinder shell AUVs. Comparison of the flow noise measurement experiment and the sensor sensitivity measurement experiment revealed the following insights: (1)The riblet skin's reduction in flow noise observed during the flow noise measurement experiment can be attributed to the physical properties of the processed material, which hinder sound propagation, rather than a decrease in the turbulent boundary layer intensity. (2) The placoid-scale skin diminishes the flow noise by attenuating the turbulent boundary layer intensity, with an effective reduction within the 0–450 Hz range. (3) Compared to smooth surfaces, the placoid-scale skin more effectively attenuated flow noise by about 5 dB, while maintaining better sensor performance.

Author Contributions: In the research process of this article, the contributions of several authors are as follows: conceptualization, M.C.; methodology, K.S. and L.Y.; software, M.C.; validation, M.C. and B.W.; formal analysis, M.C. and B.W.; investigation, M.C.; data curation, B.W. and M.C.; writing—original draft preparation, M.C.; writing—review and editing, B.W. and K.S.; visualization, M.C.; supervision, K.S. and L.Y.; project administration, K.S. and L.Y.; funding acquisition, Z.Z., K.S. and L.Y. All authors have read and agreed to the published version of the manuscript.

Funding: This research received no external funding.

Institutional Review Board Statement: Not applicable.

Informed Consent Statement: Not applicable.

Data Availability Statement: Data are contained within the article.

Conflicts of Interest: The authors declare no conflicts of interest.

References

1. Siregar, S.; Trilaksono, B.R.; Hidayat, E.M.I.; Kartidjo, M.; Habibullah, N.; Zulkarnain, M.F.; Setiawan, H.N. Design and construction of hybrid autonomous underwater glider for underwater research. *Robotics* **2023**, *12*, 8. [CrossRef]
2. Wrzos-Kaminska, M.; Pettersen, K.Y.; Gravdahl, J.T. Path following control for articulated intervention-AUVs using geometric control of reduced attitude. *IFAC-PapersOnLine* **2019**, *52*, 192–197. [CrossRef]
3. d'Amore-Domenech, R.; Raso, M.A.; Villalba-Herreros, A.; Santiago, Ó.; Navarro, E.; Leo, T.J. Autonomous underwater vehicles powered by fuel cells: Design guidelines. *Ocean. Eng.* **2018**, *153*, 387–398. [CrossRef]
4. Whitt, C.; Pearlman, J.; Polagye, B.; Caimi, F.; Muller-Karger, F.; Copping, A.; Spence, H.; Madhusudhana, S.; Kirkwood, W.; Grosjean, L.; et al. Future vision for autonomous ocean observations. *Front. Mar. Sci.* **2020**, *7*, 697. [CrossRef]
5. Wang, X.; Wang, Y.; Wang, P.; Yang, S.; Niu, W.; Yang, Y. Design, analysis, and testing of petrel acoustic autonomous underwater vehicle for marine monitoring. *Phys. Fluids* **2022**, *34*, 037115. [CrossRef]
6. Ma, L.; Lin, K.; Fan, D.; Wang, J.; Triantafyllou, M.S. Flexible cylinder flow-induced vibration. *Phys. Fluids* **2022**, *34*, 011302. [CrossRef]
7. Berglund, B.; Hassmen, P.; Job RF, S. Sources and effects of low-frequency noise. *J. Acoust. Soc. Am.* **1996**, *99*, 2985–3002. [CrossRef] [PubMed]

8. Piskur, P.; Szymak, P.; Jaskólski, K.; Flis, L.; Gąsiorowski, M. Hydroacoustic system in a biomimetic underwater vehicle to avoid collision with vessels with Low-Speed propellers in a controlled environment. *Sensors* **2020**, *20*, 968. [CrossRef] [PubMed]
9. Wei, Y.; Li, M.; Liu, J.; Chen, Y.; Qu, F.; Zhang, M. Flow noise and its suppression in exposed hydrophone. *Appl. Acoust.* **2021**, *182*, 108190. [CrossRef]
10. Sun, T.; Shen, J.; Jiang, Q.; Li, Y. Dynamics analysis of high-speed water entry of axisymmetric body using fluid-structure-acoustic coupling method. *J. Fluids Struct.* **2022**, *111*, 103551. [CrossRef]
11. Piskur, P.; Szymak, P. Algorithms for passive detection of moving vessels in marine environment. *J. Mar. Eng. Technol.* **2017**, *16*, 377–385. [CrossRef]
12. Fan, Y.; Lyu, P.; Zhan, D.; Ouyang, K.; Tan, X.; Li, J. Surrogate model-based multi-objective design optimization for air-cooled battery thermal management systems. *Eng. Appl. Comput. Fluid Mech.* **2022**, *16*, 1031–1047.
13. Hu, F.; Huang, Y.; Xie, Z.; Yu, J.; Wang, Z.; Qiao, J. Conceptual design of a long-range autonomous underwater vehicle based on multidisciplinary optimization framework. *Ocean. Eng.* **2022**, *248*, 110684. [CrossRef]
14. Piskur, P. Side Fins Performance in biomimetic unmanned underwater vehicle. *Energies* **2022**, *15*, 5783. [CrossRef]
15. Li, W.; Roggenkamp, D.; Paakkari, V.; Klaas, M.; Soria, J.; Schroeder, W. Analysis of a drag reduced flat plate turbulent boundary layer via uniform momentum zones. *Aerosp. Sci. Technol.* **2020**, *96*, 105552. [CrossRef]
16. Guo, T.; Fang, J.; Zhang, J.; Li, X. Direct numerical simulation of shock-wave/boundary layer interaction controlled with convergent–divergent riblets. *Phys. Fluids* **2022**, *34*, 086101. [CrossRef]
17. Joslin, R.D.; Thomas, R.H.; Choudhari, M.M. Synergism of flow and noise control technologies. *Prog. Aerosp. Sci.* **2005**, *41*, 363–417. [CrossRef]
18. Gillcrist, M.C.; Reidy, L.W. *Drag and Noise Measurements on an Underwater Vehicle with a Riblet Surface Coating*; Naval Ocean Systems Center (NOSC): San Diego, CA, USA, 1989.
19. Shi, X.; Song, B.; Shi, Z. Experimental study on flow noise reduction by riblets. *Northwestern Polytech. Univ. J.* **1997**, *15*, 395–398.
20. Chen, D.; Liu, Y.; Chen, H.; Zhang, D. Bio-inspired drag reduction surface from sharkskin. *Biosurface Biotribology* **2018**, *4*, 39–45. [CrossRef]
21. Luo, Y.H.; Li, X.; Zhang, D.Y.; Liu, Y.F. Drag reducing surface fabrication with deformed sharkskin morphology. *Surf. Eng.* **2016**, *32*, 157–163. [CrossRef]
22. Fu, Y.F.; Yuan, C.Q.; Bai, X.Q. Marine drag reduction of shark skin inspired riblet surfaces. *Biosurface Biotribology* **2017**, *3*, 11–24. [CrossRef]
23. Zhang, Y.; Chen, H.; Fu, S.; Dong, W. Numerical study of an airfoil with riblets installed based on large eddy simulation. *Aerosp. Sci. Technol.* **2018**, *78*, 661–670. [CrossRef]
24. Kaakkunen, J.J.; Tiainen, J.; Jaatinen-Värri, A.; Grönman, A.; Lohtander, M. Nanosecond laser ablation of the trapezoidal structures for turbomachinery applications. *Procedia Manuf.* **2018**, *25*, 435–442. [CrossRef]
25. Meng, K.Y.; Zhang, H.X.; Shi, Y.L.; Pan, Y.C. Numerical study for turbulent flow of drag and flow noise with wavy wall. *J. Shanghai Jiaotong Univ. (Sci.)* **2011**, *16*, 45–54. [CrossRef]
26. Dang, Z.; Mao, Z.; Tian, W. Reduction of hydrodynamic noise of 3d hydrofoil with spanwise microgrooved surfaces inspired by sharkskin. *J. Mar. Sci. Eng.* **2019**, *7*, 136. [CrossRef]
27. Yang, Y.; Song, X.; Li, X.; Chen, Z.; Zhou, C.; Zhou, Q.; Chen, Y. Recent progress in biomimetic additive manufacturing technology: From materials to functional structures. *Adv. Materials.* **2018**, *30*, 1706539. [CrossRef] [PubMed]
28. Dai, W.; Alkahtani, M.; Hemmer, P.R.; Liang, H. Drag-reduction of 3D printed shark-skin-like surfaces. *Friction* **2019**, *7*, 603–612. [CrossRef]
29. Yao, H.L.; Zhang, H.X.; Liu, H.T.; Jiang, W.C. Numerical study of flow-excited noise of a submarine with full appendages considering fluid structure interaction using the boundary element method. *Eng. Anal. Bound. Elem.* **2017**, *77*, 1–9. [CrossRef]
30. Tu, J.F.; Gan, L.; Ma, S.J.; Zhang, H. Flow noise characteristics analysis of underwater high-speed vehicle based on LES/FW-H coupling model. *Acoust Aust.* **2019**, *47*, 91–104. [CrossRef]
31. Brekhovskikh, L.M.; Godin, O.A. *Acoustics of Layered Media II: Point Sources and Bounded Beams*; Springer Science & Business Media: Berlin/Heidelberg, Germany, 2013.
32. Jensen, F.B.; Kuperman, W.A.; Porter, M.B.; Schmidt, H.; Tolstoy, A. *Computational Ocean Acoustics*; Springer Science& Business Media: Berlin/Heidelberg, Germany, 2011.
33. Chen, H.; Zhang, X.; Che, D.; Zhang, D.; Li, X.; Li, Y. Synthetic effect of vivid shark skin and polymer additive on drag reduction reinforcement. *Adv. Mech. Eng.* **2014**, *6*, 425701. [CrossRef]
34. Dong, H.; Wu, Z.; Chen, D.; Tan, M.; Yu, J. Development of a Whale-Shark-Inspired gliding robotic fish with high maneuverabil-ity. *IEEE/ASME Trans. Mechatron.* **2020**, *25*, 2824–2834. [CrossRef]
35. Afroz, F.; Lang, A.; Habegger, M.L.; Motta, P.; Hueter, R. Experimental study of laminar and turbulent boundary layer separation control of shark skin. *Bioinspiration Biomim.* **2016**, *12*, 016009. [CrossRef] [PubMed]
36. Wen, L.; Weaver, J.C.; Lauder, G.V. Biomimetic shark skin: Design, fabrication and hydrodynamic function. *J. Exp. Biol.* **2014**, *217*, 1656–1666. [CrossRef] [PubMed]
37. Liu, B. Studies on the Morphological Dimensions of the Riblet Surface of Fast Swimming Sharks. Ph.D. Thesis, Qingdao University of Science and Technology, Qingdao, China, 2008.

38. Liu, Y.; Gu, H.; Jia, Y.; Liu, J.; Zhang, H.; Wang, R.; Zhang, B.; Zhang, H.; Zhang, Q. Design and preparation of biomimetic polydimethylsiloxane (PDMS) films with superhydrophobic, self-healing and drag reduction properties via replication of shark skin and SI-ATRP. *Chem. Eng. J.* **2019**, *356*, 318–328. [CrossRef]
39. Felten, F.N.; Fautrelle, Y.R.; Terrail, Y.D.; Métais, O. Numerical modelling of electromagnetically-driven turbulent flows using LES methods. *Appl. Math. Model.* **2004**, *28*, 15–27. [CrossRef]

Disclaimer/Publisher's Note: The statements, opinions and data contained in all publications are solely those of the individual author(s) and contributor(s) and not of MDPI and/or the editor(s). MDPI and/or the editor(s) disclaim responsibility for any injury to people or property resulting from any ideas, methods, instructions or products referred to in the content.